Journal of Materials Science: Materials in Electronics (2018) 29:17022–17037
https://doi.org/10.1007/s10854-018-9799-0

Direct photo-oxidation and superoxide radical as major responsible for dye photodegradation mechanism promoted by TiO_2–rGO heterostructure

Gabriela Byzynski[1] · Diogo P. Volanti[2] · Cauê Ribeiro[3] · Valmor R. Mastelaro[4] · Elson Longo[5]

Received: 24 May 2018 / Accepted: 1 August 2018 / Published online: 4 August 2018

Abstract
The increase in photocatalytic activity of reduced graphene oxide–TiO_2 heterostructures under ultraviolet and visible illumination is already well known, as the photocatalyst mechanism modifications with heterostructure formation. However, which step in the degradation mechanism is modified with reduced graphene oxide–TiO_2 heterostructure formation has been not demonstrated yet. These specific modifications are caused by the alteration in reactive oxygen species production. In this way, the goal of this study is defined which reactive oxygen species are produced by reduced graphene oxide–TiO_2 heterostructure in the photocatalytic mechanism. A fast synthesis method to obtain this heterostructure by the microwave-assisted solvothermal method is presented, obtaining an improvement of photocatalytic efficiency, under UV and visible illumination. The non-hydrolytic method favors a better distribution of TiO_2 nanoparticles around the reduced graphene oxide structure and inhabits the charge carrier recombination, showing a faster electron transfer than TiO_2 samples. The RhB discoloration mechanism confirms that the reduced graphene oxide presence modifies the main reactive oxygen species produced. Under UV illumination, O_2H^* radical is the dominant reactive oxygen species produced by TiO_2. For the heterostructure, the direct oxidation by oxygen vacancy is the primary mechanism step. Under visible illumination, O_2H^* is the main reactive oxygen species for both materials. The results present a better understanding of principal reasons related to the improvement in photocatalytic activity and could be useful in semiconductor heterostructure design.

1 Introduction

Graphene oxide (GO) and reduced-GO (rGO) are excellent candidates to anchor semiconductors nanocrystals due to the presence of functional groups in GO surface and offer desirable efficiency in electron–hole pairs separation [1–10]. Reduced graphene oxide (rGO)/WO_3 heterostructures have a better UV photocatalytic activity in the degradation of the methylene blue dye at the 15% RGO mass ratio in WO_3 than others rGO–WO_3 proportion (from 6 to 20%) [11]. Long et al. [12] reported the photocatalytic activity of graphene oxide/TiO_2 (0.8 wt%) compounds in the photodegradation of dye under visible light, assigning the photocatalytic activity in the visible region to the *p*–*n* junction heterostructure formed between rGO and TiO_2. The highest photocatalytic activity in the treatment of water containing high salinity levels and different compositions of recalcitrant organic matter is obtained for a rGO/TiO_2 weight ratio of about 10% [13]. The 10% of rGO/TiO_2 is also presented with the better condition for Rhodamine 6G degradation under UV illumination.

The increase in photocatalytic activity can be attributed to the excellent charge transport property of the rGO, which is thermodynamically favored. Also, rGO has high load mobility, and the charges transport through the rGO structure is relatively fast and may be useful in oxidation–reduction

Electronic supplementary material The online version of this article (https://doi.org/10.1007/s10854-018-9799-0) contains supplementary material, which is available to authorized users.

✉ Gabriela Byzynski
gabi.byzynski@gmail.com

[1] IQ, UNESP, São Paulo State University, Av. Prof. Francisco Degni, 55 - Jardim Quitandinha, Araraquara, SP 14800-900, Brazil

[2] IBILCE, UNESP, São Paulo State University, São José do Rio Preto, SP, Brazil

[3] Embrapa Instrumentation, São Carlos, SP, Brazil

[4] Physics Institute of São Carlos, USP, São Carlos, SP, Brazil

[5] DQ, UFSCar, Federal University of São Carlos, São Carlos, SP, Brazil

reactions [14]. However, the properties of the composite obtained are not a simple superposition of the properties of individual constituents, as the strong surface interactions among the narrow semiconductors nanoparticles occur [15]. The heterostructures formation of different semiconductor oxides allows absorbing a broad range of wavelength (UV and visible light) and succeeding electron–hole pair separation, increasing photocatalytic activity [16].

In this way, this study looks to define which reactive oxygen species are responsible for photocatalytic degradation with TiO_2–rGO heterostructure, to understand better organic contaminants degradation mechanism and factors that modify the heterostructure photocatalytic activity. A fast synthesis method to obtain TiO_2 heterostructures with rGO (TiO_2–rGO) by the microwave-assisted solvothermal method (MAS), with improved photocatalytic activity compared with TiO_2, was proposed. The anatase crystalline phase samples were characterized by X-ray diffraction and high-resolution transmission electron microscopy (HRTEM), and the reduced characteristic of rGO was confirmed by Raman spectroscopy. Field emission scanning electron microscopy and HRTEM confirms the interaction between rGO sheets and TiO_2 nanoparticles. The TiO_2–RGO heterostructure shows a different optical behavior obtained by diffusive reflectance spectroscopy. Photo-carrier transfer and separation were also evaluated by photoluminescence results and cyclic voltammograms. Finally, the photocatalytic mechanism modification of TiO_2–rGO heterostructure compared with TiO_2 in the RhB photo-degradation mechanism was confirmed through scavenger solutions. The rGO insertion alters the reactive oxygen intermediate, promoting an increase in photocatalytic activity, under UV and visible illumination. The correlation between structural and electronic properties and the improved photocatalytic activity of TiO_2–rGO heterostructure was also discussed.

2 Materials and methods

2.1 GO synthesis

All of the chemical reagents were analytical grade. Graphene oxide (GO) was obtained by the Hummers method [17, 18], using natural graphite as a precursor. Thus, $NaNO_3$ (1.0 g) and graphite (1.0 g) were dissolved in 46 mL of concentrated H_2SO_4. After 30 min in an ice bath under stirring, $KMnO_4$ (6.0 g) is added slowly and remaining for 2 h under the same condition. After that, the mixture was heated to 35 °C under stirring for 2 h. Then, deionized water (46 mL) was added, and the reaction temperature was maintained at 98 °C. After 15 min, the solution was removed from heating, and 100 mL of deionized water and 20 mL of H_2O_2 (30%) were added. The dark brown solution turns yellow-brown, with a solid of the same color in suspension that can be decanted. At the end of the reaction, the mixture was centrifuged at 3500 rpm for 10 min, until the supernatant presents a negative sulfate test with the addition of barium salt solution.

2.2 TiO_2 synthesis

TiO_2 nanoparticles were obtained through the MAS method, using titanium isopropoxide (Sigma-Aldrich) as Ti precursor. 2.1 ml of titanium isopropoxide were added in 30 mL of distilled water, with continuous stirring. After 10 min, acetic acid (0.35 mol L^{-1}) was inserted until pH reach 3.0. Distilled water was added until completed 60 mL of solution and inserted into a polytetrafluoroethylene (PTFE) hydrothermal reactor for 80 min at 140 °C assisted microwave-aided device for hydrothermal synthesis [19]. The resulted suspension was centrifuged five times at 7000 rpm for 10 min, and dry, at 80 °C, all night.

2.3 TiO_2–rGO heterostructure synthesis

TiO_2–rGO heterostructure sample was also synthesized by the MAS method, using dimethylformamide (DMF) and isopropyl alcohol as priority solvents. 20.0 mg of GO was solubilized in 20 mL of DMF in an ultrasonic bath. In the same solution, 2.1 mL of titanium isopropoxide was added and remaining under constant stirring at 100 °C during 30 min. After that, 20 mL of isopropyl alcohol, 20 mL of deionized water, and 1.26 mL of acetic acid were added and stirred for 10 min. Afterward, the resulting solution was inserted in microwave-assisted polytetrafluoroethylene (PTFE) hydrothermal reactors for hydrothermal synthesis during 80 min at 160 °C. This sample was named as TiO_2–rGO, and the content of GO is 5.0 wt%.

2.4 Characterization techniques

Samples were characterized by microscopic, spectroscopic and crystallographic techniques. Field emission scanning electron microscopy (FE-SEM) (JEOL Microscope Model JSM 6701F) and transmission electron microscopy (TEM) (FEI microscope model Tecnai F20) were used to define morphology and size of the samples. X-ray dispersion (XRD) (Miniflex 300 Rigaku) was employed with a Cu anode (λCu-K_α = 0.154 nm) in the range of $2\theta = 20°$–$70°$ at 2° min^{-1} step was used to evaluate crystalline phase structure. The Brunauer–Emmett–Teller (BET) method obtained through N_2 physisorption (Micromeritics Gemini VII) was employed to obtain the surface areas (SA) of synthesized samples. UV/Vis diffuse reflectance spectrophotometer (UV–Vis–NIR Cary 5G spectrophotometer) and Raman spectrometer (Renishaw, in-Via model) were used, with 633 nm laser to evaluate the optical proprieties

of samples. The photoluminescence (PL) studies of solid samples were performed using a fluorescence spectrometer (Perkin Elmer LS 55) with a krypton multiline laser with an excitation wavelength of 280 nm. X-ray Photoelectron Spectroscopy (XPS) was performed using a Scienta Omicron ESCA + model equipment with a high-performance hemispheric analyzer (EA 125) adjusted to pass energy of 50 eV, and a monochromatic Al K_α ($h\nu = 1486.6$ eV) radiation was used as the excitation source. The operating pressure in the ultrahigh vacuum chamber (UHV) during analysis was around 2×10^{-9} mbar. Energy steps of 0.5 eV and 0.05 eV were used for the survey and high-resolution spectra, respectively. The binding energies were measured in reference to the C 1s peak at 284.5 eV. Thermogravimetric-differential thermal analysis (TG-DTA) was carried out on a TGA/DSC instrument of Shimadzu DTG-60H in air flow at a heating rate of 10 °C/min.

Electrochemical measurements were carried out in a conventional three-electrode system, connected to a computer-controlled potentiostat (MPG-01- Microchimica). The three-electrode system contained a thin film electrode as the working electrode, Pt wire as the counter electrode, and a Saturated Calomel Electrode (SCE) as the reference electrode. The TiO_2 and RGO–TiO_2 thin film electrode were produced by dip coating an ITO (indium-tin oxide) substrate with the solution of synthesized materials dispersed in ethylene glycol (2 mg/mL). The area of thin film electrodes were 270.75 mm^2. Cyclic voltammograms were measured in a 0.005 mol L^{-1} aqueous solution of potassium ferricyanide ($K_3Fe(CN)_6$)(Merck), with a scan rate of 50 mV s^{-1}.

2.5 Photocatalytic procedures

The photocatalytic behavior of samples was obtained by the discoloration percentage of dye (Rhodamine-B (RhB) (2.5 mg L^{-1})) solution [UV–Vis Spectrophotometer (UV-2600 Shimadzu)]. In separated beaker, 2 mg of each samples were dispersed in 20 mL of RhB solution, under magnetic stirring, and placed in a reactor with UV-C illumination (TUV Philips, 15 W, with maximum intensity) or visible light (six Philips lamps, 15 W, and maximum intensity at 440 nm), at constant temperature of 25 °C. A UV–Vis spectrophotometer (Shimadzu-UV-1601 PC spectrophotometer) was used to monitor the optical absorption of RhB solution throughout the experiment (2 h). Control, without the semiconductor materials, only with RhB solution, was also performed (photolysis). The RhB adsorption kinetic was also conducted with the same apparatus and condition used for photocatalytic experiment without illumination (dark condition).

The photocatalytic mechanisms under UVC and visible irradiation were studied using different scavenger substances for each sample. The substances used were sec-butanol ($C_4H_{10}O$, 200.0 mmol L^{-1}, Merck®) (OH radicals scavenger), 2Na–EDTA ($C_{10}H_{16}N_2O_8$, 200.0 mmol L^{-1}, Synth®) (hole quencher) and p-benzoquinone ($C_6H_4O_2$, 203.0 mg L^{-1}, Merck®) (superoxide radical scavenger). The kinetic results are described as an average of three experiments, and it showed the standard deviations for each measurement and kinetic rates, as the R-squared.

3 Results and discussion

3.1 Structure and morphology characterization of photocatalysts

Surface morphology of the TiO_2 nanoparticles shaped pristine, and TiO_2–rGO heterostructure was characterized by FE-SEM in Fig. 1. The TiO_2 nanoparticles show spherical particles agglomeration with various size distribution, with 6.0 nm average size (Fig. 1a), classified as nanoparticles due to the small average size. The same morphology with similar size is observed for TiO_2 obtained through sol–gel methods [20, 21] and, through oxidant peroxide method, TiO_2 describes the cylindrical architecture of nanorods [22]. Trough microwave assisted hydrothermal synthesis, the influence of temperature and microwaves intensity promote the water diffusion away from Ti^{4+} precursors, inducing an amount of crystal nucleus on the solution and, consequently, diminishing particles size. To decrease the system energy and due to the adequate surface charges, TiO_2 nanoparticles tend to agglomerate. The HRTEM images of TiO_2 nanoparticles in Fig. 1b confirmed agglomeration of crystalline spherical nanoparticles. Interplanar lattice spacing of TiO_2 is identifying (Fig. 1b) as 0.36 nm and 0.25 nm, corresponding to the (101) and (103) planes of anatase phase of TiO_2, respectively, suggesting anatase as the primary crystalline phase.

Figure 1c is depicted the FE-SEM images of the TiO_2–rGO sample as TiO_2 nanoparticles agglomerations all over the rGO surface, similar to TiO_2 sample images. The synthesis condition, mainly the solvent characteristic, alters the growth mechanism. The acceptable solubility of GO in DMF solvent (an organic solvent) and, the satisfactory solubility of the Ti^{4+} precursor in isopropyl alcohol enable the formation of clusters with an increase of defects density as oxygen vacancy. Once Ti^{4+} precursor solution was dispersed in GO solution, the color of Ti^{4+} solution modified from white to light brown, indicating an interaction between oxygen vacancy ($[TiO_5.V_o]$) from Ti^{4+} precursor and electrons from GO particles. The interaction is caused mainly by oxygenated functional groups on GO surface, where is initiated the nucleation formation during the synthesis method, with temperature and microwave irradiation, and TiO_2 nanoparticles

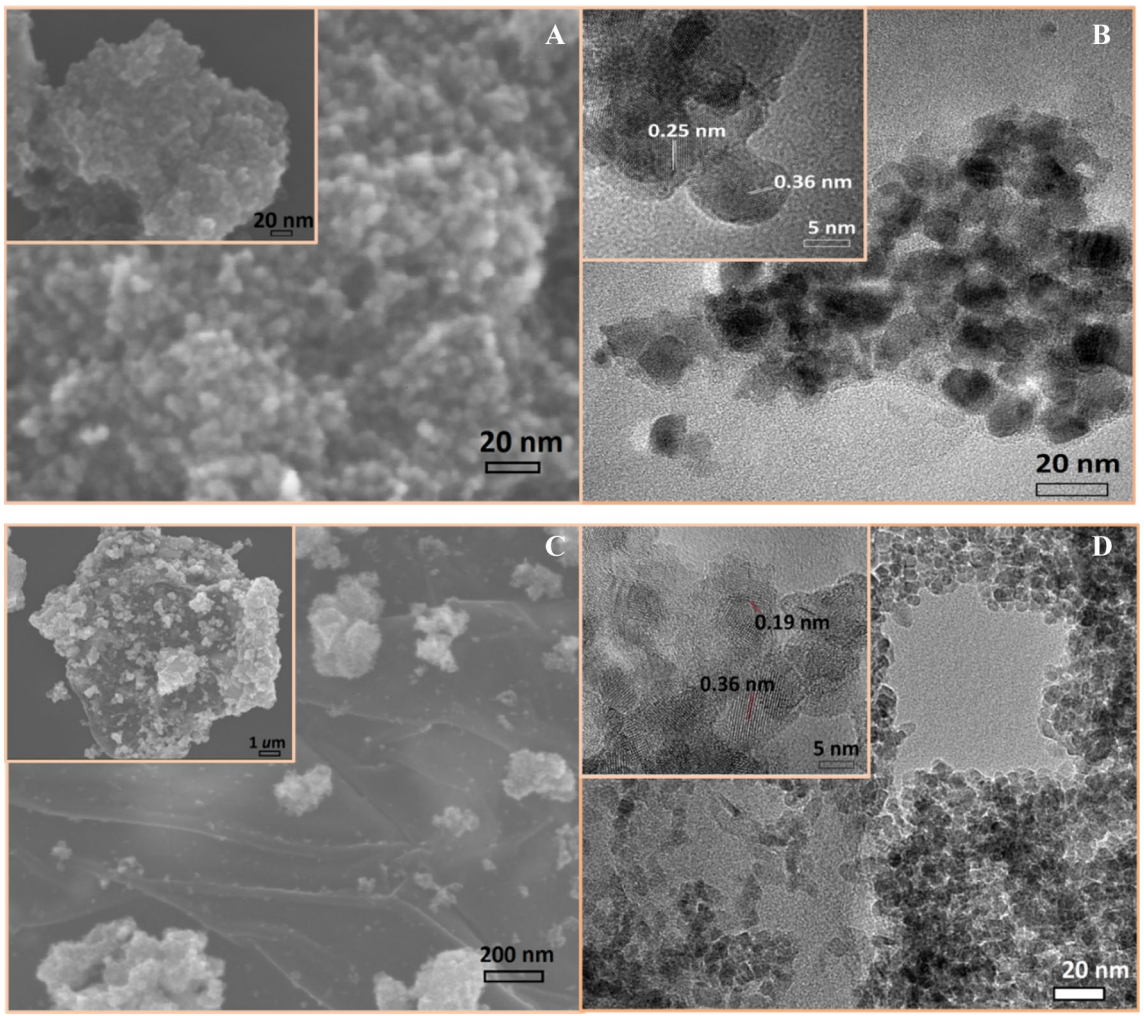

Fig. 1 FE-SEM images of TiO_2 (**a**) and TiO_2 RGO (**c**), HRTEM images of TiO_2 (**b**) and TiO_2–rGO (**d**)

formation/crystallization. In the same way in which the synthesis condition promotes TiO_2 nanoparticles formation, the microwave treatment helps the GO reduction by Ti powders, creating then a heterostructure between TiO_2 and rGO [23].

The growth of TiO_2 nanocrystals with different rGO sheet morphologies are attributed to different reducing abilities of the $[TiO_5.V_o]$ complex cluster as a result of the hydrolysis in solution. For the solvothermal method, similar results of TiO_2–rGO heterostructure sample are observed using $TiCl_4$ as Ti precursor solution and ethyl alcohol [24]. The growth of TiO_2 nanospheres without growth promoter reagent, uniformly deposited on GO sheets, is also reported using titanium sulfate as Ti precursor [5]. The hydroxyl functional groups in GO sheets act as heterogeneous nucleation sites for anchoring the $[TiO_5.V_o]$ complex clusters, resulting in well distributed TiO_2 nanospheres. Wang et al. [23] obtained TiO_2–rGO heterostructure samples using a two-step synthesis method. The first one is the synthesis of TiO_2 in the hydrothermal method followed by the microwave-assisted method to disperse and reduce GO leaves.

HRTEM images of TiO_2–rGO heterostructure sample in Fig. 1d showed that TiO_2 nanoparticles are distributed all over the rGO sheets, confirming the TiO_2 and rGO interaction, which is essential in a semiconductor heterostructure. Structures transparency confirms the nanometric thickness of rGO structures through microscopy electron bean. TiO_2 distribution over the rGO sheets confirms the TiO_2 growth mechanism through heterogeneous nucleation sites for anchoring the $[TiO_5V_o]$ complex clusters. The 0.36 nm interplanar lattice distance was observed, corresponding to (101) plane of TiO_2 anatase and similar with TiO_2 sample. Other interplanar distance was observed as 0.19 nm, corresponding to (200) plane of TiO_2 anatase, confirming anatase as the main crystalline phase TiO_2–rGO heterostructure sample.

Figure 2a shows the X-ray diffraction patterns (DRX) of TiO_2 and TiO_2–rGO heterostructure samples, indexed as TiO_2 crystalline phase anatase (JCPDF 21 1272) for

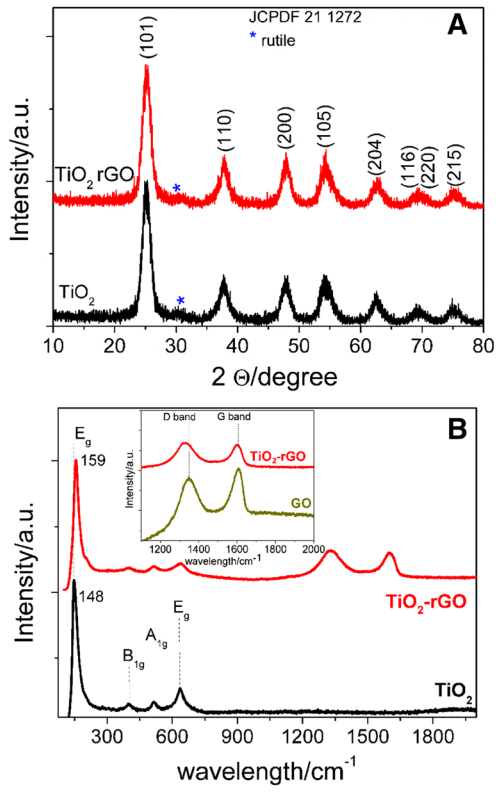

Fig. 2 **a** X-ray diffraction of TiO_2 and TiO_2–rGO samples indexed with JCPDF 21 1272. **b** Raman spectra of TiO_2 and TiO_2–rGO samples

Table 1 Crystallite size (nm), specific surface area (SSA, $m^2\ g^{-1}$) and band gap value (eV) of TiO_2 and TiO_2–rGO samples

Samples	Crystallite size-*d* (nm)	SSA–BET ($m^2\ g^{-1}$)	Band gap energy (eV)
TiO_2	5.09	193.96	3.24
TiO_2–rGO	5.30	180.78	3.20

both samples, endorsing the HRTEM interplanar distances results. The presence of GO in 5% (w/w) does not alter the formation of the main crystalline phase anatase even induces the formation of other crystalline phases. Other authors also cited the anatase crystalline phase retention with the introduction of GO in TiO_2 samples [27].

Due to the spherical characteristic of TiO_2 nanoparticles presented by FE-SEM images, the average crystallite size (***d***), obtained by Scherrer equation [28], as well as the specific surface area estimated by N_2 physisorption using the BET methods, are depicted in Table 1. For Scherer equation calculation, only the main anatase TiO_2 crystallographic peak (~ 25°) was utilized for each sample. For ***d*** results, TiO_2 and TiO_2–rGO heterostructure samples are classified as nanoparticles, confirmed the FE-SEM average size results, due to ***d*** values range from 5.09 to 5.30 nm, for TiO_2 and TiO_2–rGO heterostructure samples, respectively. The presence of GO in the precursor solution promotes a slight increase in crystallite size of TiO_2. The rGO presence decreased the BET specific surface area (SSA) compared with TiO_2 samples. The nanoparticles observed in HRTEM images are not a single crystal, and each particle corresponds to an aggregate of some small crystallites.

Raman spectra in Fig. 2b produced the direct evidence for TiO_2–rGO heterostructure formation. Typical Raman spectra of TiO_2 samples with distinct peaks attributed to anatase phase is showed with the Raman active modes of anatase phase with E_g, B_{1g}, A_{1g}, and E_g symmetries. Raman spectrum of GO shows two main intense peaks at 1335 cm^{-1} (D band) and 1590 cm^{-1} (G band). For TiO_2–rGO heterostructure, Raman spectrum presents the active modes of anatase phase, as well as D band and G band of GO. However, a peak shift for anatase peaks and D and G bands are observed. For the TiO_2 sample, the main E_g vibration peak is located at 148 cm^{-1} and for TiO_2–rGO heterostructure sample is blue-shifted (159 cm^{-1}). The same behavior is noticed for D and G band.

The typical D band of GO (1349 cm^{-1}) is related to structural imperfections created in GO reduction methods, and G band (1608 cm^{-1}) is attributed to E_{2g} photon scattering of sp^2 carbon [25]. The reduction method used here is the microwave treatment, which could induce the GO reduction to rGO during heterostructure formation. Those D and G band for TiO_2–rGO heterostructure sample shifted to 1327 and 1600 cm^{-1}, respectively, compared with TiO_2 sample. The intensity ratio of D and G band (I_D/I_G) for GO sample (0.77) indicates the presence of a significant amount of sp^2 carbon in GO material. For TiO_2–rGO heterostructure sample, the I_D/I_G increased (1.08) and is associated with more structural imperfections produced by the functional groups introduced to the GO material during the microwave synthesis method [25].

The optical behavior of the samples was also evaluated by diffuse reflectance spectroscopy (DRS), and the results are presented in Fig. 3. It can be observed that the optical behavior changes entirely with the TiO_2–rGO heterostructure formation, decreasing the gap, similar behavior is observed for other materials [26–28].

In the inset of Fig. 3, Kubelka Munk Function versus band gap energy of the respective samples is presented, and it is possible to determine the band gap energy value of each sample, presented in Table 1. A change is observed for heterostructure and TiO_2 sample, slightly reducing the band gap value of the sample, and confirming the effective coupling between rGO and TiO_2 particles by the proposed method. This change could influence the photocatalytic activity of the samples, especially under visible light.

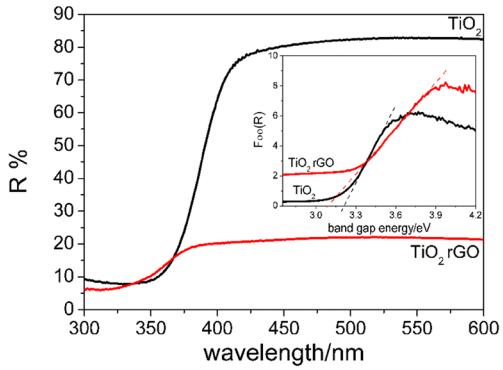

Fig. 3 UV–Vis diffusive reflectance spectra of TiO_2 and TiO_2–rGO samples. Insert Kubelka Munk function versus band gap energy of TiO_2 and TiO_2–rGO samples

The chemical states and element binding energies of TiO_2 and TiO_2–rGO heterostructure samples were studied by measuring the survey and high-resolution XPS spectra. The XPS survey scan (Fig. 4a) confirmed the presence of titanium, oxygen, and carbon as the main elements of both samples. The typical high-resolution spectra of C (Fig. 4b) were deconvoluted in four peaks. For TiO_2 sample, the peaks at 284.5 and 285.6 eV (Table 1—SI) were assigned to C=C and C–C energy binding, respectively, from adventitious carbon. For TiO_2–rGO heterostructure sample, the respective peaks were fitted at 284.4 and 285.9 eV. The peaks assigned for hydroxyl carbon (C–O) and carboxyl carbon (O–C=O) have been adjusting at 288.1 and 288.9 eV for TiO_2 and 287.8 and 288.7 eV for TiO_2–rGO heterostructure [29].

The O 1s high-resolution spectra were similar for TiO_2 and TiO_2–rGO heterostructure samples, which were deconvoluted in three central peaks. For TiO_2 sample, 529.0; 530.9; and 532.6 eV peaks were assigned to Ti–O, hydroxyl groups (O–H) and, adsorbed water (H–O–H) binding energy, respectively. For TiO_2–rGO heterostructure sample, the peaks fit at 529.3; 530.7; and 532.3 eV. The oxygen content for TiO_2 and TiO_2–rGO heterostructure was also similar as 29.93 and 30.37% (Table 1—SI), respectively, indicating that there is no evidence of chemical states modifications in relation with oxygen content between both samples [25, 30, 31]. Although XPS results do not show a reduction behavior of TiO_2–rGO heterostructure sample, Raman results confirm that the heterostructure sample has reduced graphene oxide

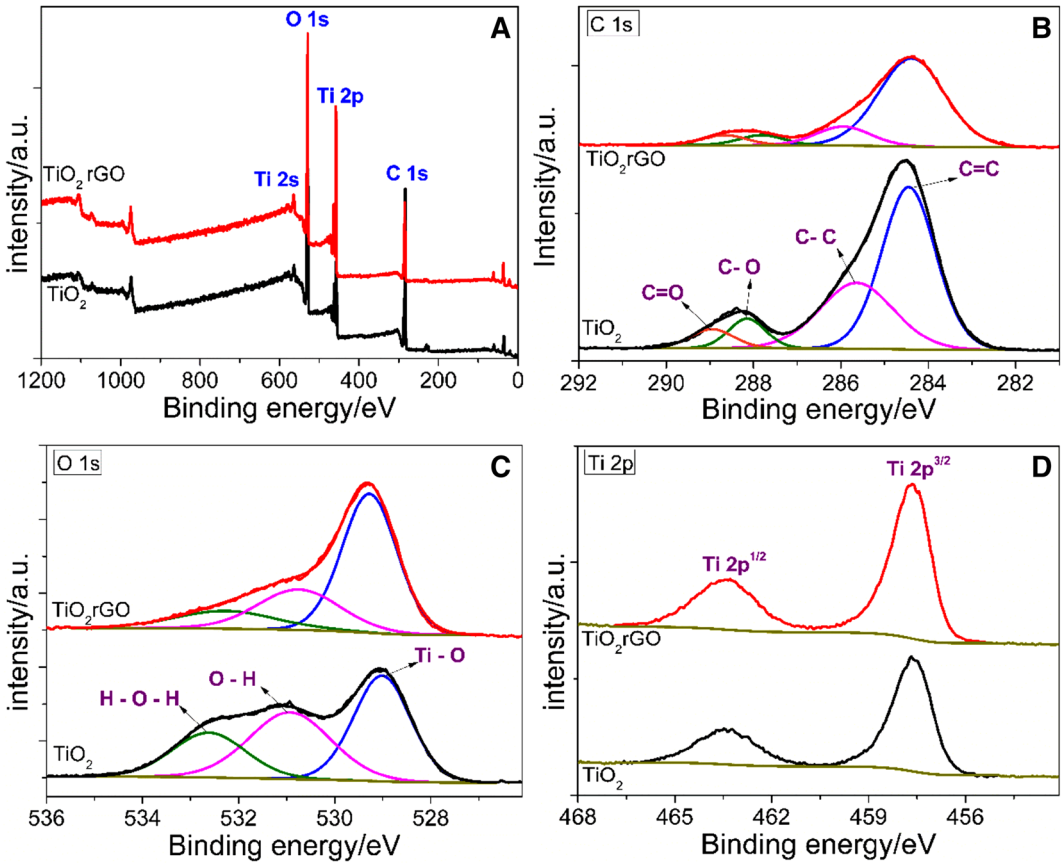

Fig. 4 **a** Survey XPS spectra, **b** C 1s XPS high-resolution spectra, **c** O 1s XPS high-resolution, **d** Ti 2p XPS high-resolution of TiO_2 and TiO_2–rGO samples

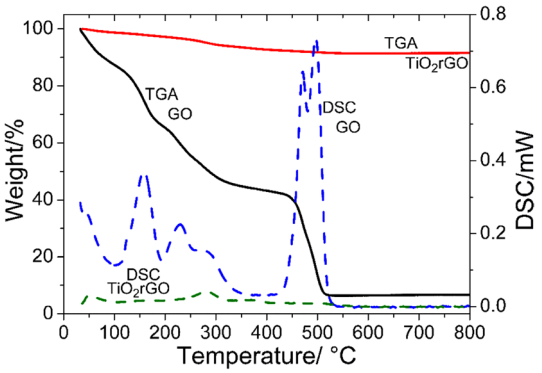

Fig. 5 TGA and DSC curves of TiO_2 and TiO_2–rGO samples

in the composition. The typical Ti 2p high-resolution spectra show two principal peaks assigned to orbital spin peaks of Ti $2p^{3/2}$ and Ti $2p^{1/2}$, at 457.6 and 463.4 eV for TiO_2, respectively, and at 457.63 and 463.34 eV for TiO_2–rGO heterostructure sample.

Thermal gravimetric analysis (TGA) and differential thermal analysis (DSC) in air atmosphere were conducted to obtain the thermal properties of GO and TiO_2–rGO (Fig. 5). As TiO_2 sample is an inorganic sample, the weight loss was not significant (not shown) while rGO sample is thermally unstable, starting losing mass since the beginning of the TG analysis. rGO sample lost around 58% of weight until 420 °C and showed a fast weight loss from 420 to 525 °C, stabilizing at 94%. DSC analysis confirms four significant TG drops in mass with exothermic peaks in 159, 203, 469, and 497 °C for rGO sample. The first mass loss process is derivate from water losses (159 °C), followed by the decomposition of the labile functional groups ($C_xO_yH_z$ species) as CO and CO_2 (203 °C). The latter two DSC exothermic peaks of the TiO_2–rGO sample (469 and 497 °C) are attributed to pyrolysis of GO carbon skeleton [32, 33]. In the case of TiO_2–rGO, the sample lost around 9% of weight until 525 °C and, afterward, the sample weight stabilized at 91.5%. The weight loss is related to the combustion of hydroxyl groups and organic substances from the precursor solution and, mainly, with the rGO degradation. Differently, from GO, the DSC of TiO_2–rGO sample presents only two exothermic peak combustion at 280 and 370 °C, associated with pyrolysis of GO carbon skeleton. The small weight loss of TiO_2–rGO sample compared with GO sample is related to the low percentage of rGO in TiO_2–rGO sample, demonstrating the decrease in thermal stability of GO after TiO_2 addition [34].

3.2 Enhancement of photocatalytic activity

The photocatalytic activity of TiO_2 and TiO_2–rGO heterostructure was tested through non-color herbicide ametryn photodegradation, under UV and visible illumination presented in Fig. 6a, b, respectively. Ametryn is a water-soluble (185 mg L^{-1}) sulfur-containing triazine herbicide with a nitrogenized aromatic ring in its chemical structure. The first photodegradation step of ametryn in acidic solution (pH 3) is the photolysis of thiol group with hemolysis of the C–S bond. Then, H abstraction occurs resulting in triazinyl radicals [35]. The thiol group photolysis promotes an intense absorption decrease in UV–Vis spectra under UV illumination, even without catalyst use (ametryn solution without TiO_2 and TiO_2–rGO heterostructure) (Fig. 1—SI), resulting in a gap in kinetic results (Fig. 6a) at initial 30 min of ametryn photodegradation. The kinetic behavior of ametryn degradation under UV and visible illumination was obtained by the maximum absorption of UV–Vis spectra in 235 nm obtained through deconvolution of UV–Vis spectra in four absorption peaks.

TiO_2–rGO heterostructure shows better photocatalyst results under UV and visible illumination compared with TiO_2. For 120 min under UV illumination, TiO_2–rGO heterostructure provokes 38% of ametryn degradation instead of 35% of TiO_2 sample, indicating a better efficiency in photogenerated charge carrier separation of TiO_2–rGO heterostructure. Reduced graphene oxide presence also could improve the adsorption behavior of TiO_2–rGO heterostructure, promoting an increase in photocatalytic activity. Although the ametryn degradation decreases under visible illumination compared with under UV illumination, TiO_2–rGO heterostructure shows the best efficiency in visible ametryn degradation, confirming a functional charge separation efficacy of TiO_2–rGO heterostructure. It is important to mention that in the non-color molecule as ametryn, the dye sensitizing mechanism does not take place under visible illumination, reducing the photocatalytic activity.

Figure 6 also shows the photocatalytic activity of the Rhodamine-B discoloration, a colorful molecule, with TiO_2 and TiO_2–rGO heterostructure samples, under UV (C) and visible illumination (D). The adsorption kinetic was conducted (Fig. 2, SI) without illumination and show less than 8% of RhB adsorption during 120 min, which indicate the catalytic effect of semiconductors material. Under UV illumination (Fig. 6c), the RhB photolysis occurs and, under visible illumination (Fig. 6d), RhB was stable until 60 min, degrading only 4% until 120 min. The presence of TiO_2 and TiO_2–rGO heterostructure samples improves the RhB discoloration under illumination, confirming the photocatalysis process occurrence. Under UV light (Fig. 6c), the TiO_2–rGO heterostructure sample shows improvement on RhB photocatalysis compared with TiO_2 sample. The TiO_2 sample reached 57% of RhB discoloration, and TiO_2–rGO heterostructure obtained 81% of RhB discoloration during 120 min. The TiO_2–rGO heterostructure formation increased the efficiency in the photocatalytic discoloration of RhB

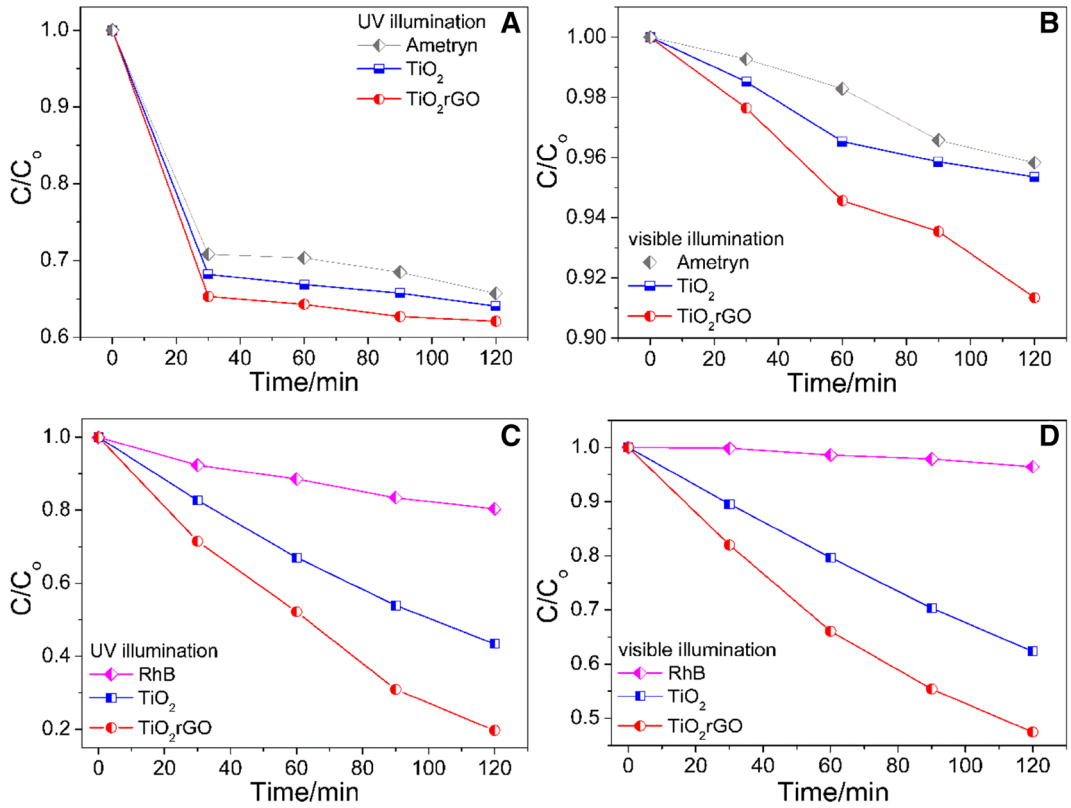

Fig. 6 Relation of C/Co versus Time of Ametryn degradation under **a** UV and **b** visible illumination. Rhodamine-B discoloration under UV (**c**) and visible (**d**) illumination

solution, promoting a better separation of photogenerated carriers than in the TiO_2 sample [36].

Zhou et al. [37] demonstrated an excellent photocatalytic activity in the degradation of methylene blue dye using TiO_2–rGO heterostructure. Authors proposed that the electron–hole pair is generated by the surface illumination of TiO_2 under UVC light. The photogenerated electrons are usually directed to the leaves of rGO and sequestered by the dissolved oxygen, facilitating the separation of the photogenerated charges. Also, the photogenerated holes react with adsorbed water or hydroxyl ions to form hydroxyl radicals, or holes are directly oxidized by the organic compounds [5].

Under visible light, the photocatalytic activity in the discoloration of RhB of TiO_2–rGO heterostructure sample presented a considerable increase compared to TiO_2. In Fig. 6d, the TiO_2 sample reached 38% of RhB discoloration, and TiO_2–rGO heterostructure obtained 53% of RhB discoloration during 120 min. GO acts as an absorbent of visible light, promoting the generation and possible efficient separations of electron/hole pair. It is important to notice that the TiO_2 distribution over rGO surface as band gap value affect the visible photocatalytic efficiency. Posa et al. [38], presented 98% of RhB discoloration under solar light irradiation with reduced GO–TiO_2 composite, attributing the photocatalytic enhancement activity compared with TiO_2 sample (42% RhB discoloration) to increased light absorption and reduction of electron/hole pair recombination with TiO_2–rGO heterostructure uses.

The RhB discoloration is classified as pseudo-first order reaction [20] due to the R-square values presented in Table 2 (UV and visible irradiation), and the photocatalytic degradation rate values (k) obtained from the kinetic relation are shown in Table 2. The heterostructure formation modifies the rate values, under UV and visible illumination, increasing the content of RhB discoloration in both cases.

The homogeneous dispersion of TiO_2 nanoparticles all over the rGO sheet, observed in FE-SEM and HRTEM

Table 2 Photocatalytic degradation rate values under UV illumination and visible irradiation obtained by TiO_2 and TiO_2–rGO heterostructure samples sample

Samples	UV illumination		Visible illumination	
	k (min s^{-1}) × 10^{-3}	R^2	k (min s^{-1}) × 10^{-3}	R^2
RhB	1.98 ± 0.085	0.993	0.42 ± 0.032	0.982
TiO_2	7.18 ± 0.166	0.998	4.02 ± 0.648	0.999
TiO_2–rGO	18.47 ± 0.127	0.992	6.78 ± 0.378	0.997

images, is an important factor which affects the improvement of photocatalytic activity of TiO_2–rGO heterostructure sample, as facilities the charge transference between the TiO_2 nanoparticle and rGO sheets. Another factor that is important to consider is the close interface of rGO and TiO_2 nanoparticle in heterostructure sample. The close interaction between [$TiO_5.V_o$] and rGO electron leads to a substantial chemical bond interaction, promoting interfacial charge carrier migration in the TiO_2–rGO heterostructure. Then, the electron/hole pair separation is more efficient, inhibiting the charge recombination process and, consequently, increasing the photocatalytic activity of TiO_2–rGO sample compared with TiO_2 [29]. The strong interaction between TiO_2 nanoparticles and the rGO sheets is also observed in the modification in Raman vibration peak characteristic to GO structure. The charge separation and electron transport of the composite materials, in the case TiO_2–rGO heterostructure, are promoted through the adequate interaction between TiO_2 nanoparticles and rGO material [39], and also improves the photocatalytic activity of TiO_2–rGO heterostructure. One important factor especially in visible RhB photodegradation in the increase of the light absorption in the visible region of heterostructure sample, which contributes to the better performance of electron/hole pair creation in larger light wavelengths and alteration of the degradation process.

All those factors that modify the photocatalytic activity of TiO_2–rGO heterostructure are based on electron/hole pair creation and/or separation, and the interfacial charge carrier migration. In this case, it is indispensable to obtain some information about charge electronic transference process to finally elucidate the improvement modification observed in photocatalytic degradation mechanism for TiO_2–rGO heterostructure compared to TiO_2 samples.

3.3 Charge electronic transference process and band diagrams

Figure 7 shows the PL spectra of both samples which were similar, indicating similar electronic structure and defects. The emission spectra show a peak of about 410 to TiO_2 and TiO_2–rGO heterostructure sample, which could be ascribed to the band edge-free excitation, attributed to an indirect transition [40]. According to Fig. 7, the intensity of photogenerated electron/hole pairs of TiO_2 sample is higher than for TiO_2–rGO heterostructure, confirming that the heterostructure formation avoids the charge recombination [41]. A lower PL intensity corresponds to lower recombination of photogenerated carriers, promoting an increase in e^-/h^+ lifetime, creating an increase in photocatalytic activity efficiency.

As confirmed by PL results, the TiO_2–rGO heterostructure avoids the charge recombination. However, the standard

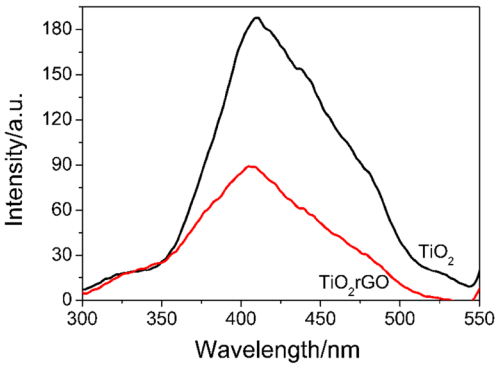

Fig. 7 Fluorescence emission spectra with excitation at 280 nm of the samples

heterogeneous rate constant, k_o, which corresponds to the rate of electron transfer in each material, was obtained by Nicholson method [42], using cyclic voltammograms (CV). CVs have been achieved with thin-film electrodes constructed with TiO_2 or TiO_2–rGO heterostructure. Figure 8a shows that the UV illumination cyclic voltammograms (photocurrent) did not modify considerably compared within the dark cyclic voltammograms for both electrodes. However, for TiO_2 sample, the UV illumination promotes an enlargement in ΔE (0.450 V vs. SCE—Table 3) compared without lighting (0.418 V vs. SCE). For TiO_2-rGO heterostructure sample, the UV illumination displays similar ΔE values (0.458 V vs. SCE) without illumination (0.479 V vs. SCE—Table 3). The illumination provokes the enlargement of ΔE values for both materials. Besides the current reduction density, the oxidation current density diminished under illumination as shown in Table 3. For k_0 calculation, the diffusion coefficients used were $D_O = D_R = 7.26 \times 10^{-6}$ cm^2 s^{-1} and k_0 values are presented in Table 3 [43]. The k_0 values were slightly close, and TiO_2–rGO heterostructure causes a decrease in electron transfer. The illumination decreases the electron transfer in electrode probably due to the increase in the recombination process.

For TiO_2–rGO heterostructure with lower rGO content than 1.0 wt%, it was demonstrated that the absorbed light by the rGO is used for creating a unique photothermal effect around the photocatalyst, promoting an increase in charge transport [44]. Although TiO_2 sample presents a slightly higher k_0 than TiO_2–rGO heterostructured sample, the recombination process is higher in TiO_2 sample than in TiO_2–rGO heterostructure. Then, the balance between electron transfer and recombination process is favorable for TiO_2–rGO heterostructure, increasing the photocatalytic efficiency.

The flat band potential (V_{fb}) could be defined as a potential that no transfer charge occurs and is encountered through Buttler equation for each semiconductor.

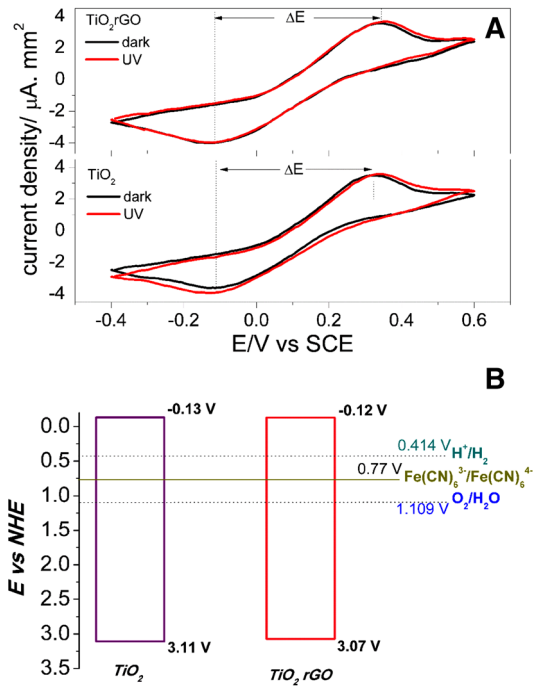

Fig. 8 **a** Cyclic voltammograms of TiO_2 and TiO_2–rGO thin-film electrodes in the dark and with UVC illumination. Scan rate = 50 mV s^{-1}; electrolyte solution: $(K_3Fe(CN)_6)$, 0.005 mol L^{-1} at ambient temperature. **b** Schematic energy band diagrams obtained through CVs and band gap values results for TiO_2 and TiO_2–rGO samples

$$j^2 = \left(\frac{2q\varepsilon\varepsilon_0 I_0^2 \alpha^2}{N_d}\right)(V - V_{fb}) \quad (1)$$

where j is the photocurrent density, N_d is the number of charges donors, q is the transferred charge per ion, ε is the permittivity of the surroundings, ε_0 is the vacuum permittivity, I_0 is the current density difference, α is the optical absorption coefficient, V is the potential [43]. The flat band potential is obtained with the x-axis onset of the square photocurrent in Fig. 7a. It is considered that V_{fb} values fit with the conduction band edge in *n*-type semiconductor materials and, then, it is possible to construct an estimate band diagram of TiO_2 and TiO_2–rGO heterostructure (Fig. 8b). The heterostructure formation TiO_2–rGO heterostructure slightly modifies the CB edge value of TiO_2, as shown in Table 3 and Fig. 8b. The band gap values were added to the CB edge to obtain valence band edge, also indicating the modification in the VB edge [45].

3.4 Structure–activity relationships and the dye photo-degradation mechanism

Until now, it was studied the structure and morphology characterization of TiO_2, and TiO_2–rGO heterostructure samples to elucidated principal reasons for TiO_2–rGO heterostructure sample shows better photocatalytic performance compared with TiO_2. This work aimed to demonstrate the influence of heterostructure formation and the modification in reactive oxygen species production (ROS). The amendment in ROS production is caused by the physical and chemical modification caused by TiO_2–rGO heterostructure formation, which changes the dye mechanism photo-degradation compared with TiO_2 sample.

The improvement of photocatalytic efficiency of TiO_2–rGO heterostructure over TiO_2 sample is caused by diverse factors, such as the homogeneous distribution of TiO_2 nanoparticles all over the rGO sheet, crystallinity, rGO reduction, and intense absorption in the visible light region. The recombination rate of photogenerated charge carrier and the rate of electron transfer (k_0) that are lower for TiO_2–rGO heterostructure than for TiO_2 are essential in photocatalytic activity efficiency.

The degradation mechanism discussed above is related explicitly to the RhB molecule, which is a well-known standard molecule for kinetic studies. Based on Kroger-Vink notations and cluster model [43], TiO_2 is described as a $[TiO_6]^x$ neutral cluster, presenting as extrinsic defects the ($[TiO_5.V_o^x]$, $[TiO_5.V_o^{\bullet}]$, $[TiO_5.V_o^{\bullet\bullet}]$), and these are linked to order–disorder effects in the electronic structure. $[TiO_5.V_o^x]$ represents the neutral oxygen vacancy, $[TiO_5.V_o^{\bullet}]$ represents the mono-ionized oxygen vacancy, and $[TiO_5.V_o^{\bullet\bullet}]$ the di-ionized oxygen vacancy.

The photocatalytic mechanism starts with the specific wavelength absorption ($h\nu$) by a TiO_2 neutral cluster

Table 3 Peak-to-peak separation (ΔE) values, the current density of oxidation and reduction obtained from Fig. 8a, the standard heterogeneous rate constant (k_0) and flat-band potential (V_{fb}) for TiO_2 and TiO_2–rGO samples

Sample	ΔE (V vs. SCE)	$i_{density}$ oxidation (μA mm^2)	$i_{density}$ reduction (μA mm^2)	$k_0 \times 10^{-2}$ (cm s^{-1})	V_{fb} (V vs. NHE)
TiO_2—dark	0.418	2.75	−2.43	2.34	
TiO_2—UV	0.450	2.60	−2.50	2.15	−0.126
TiO_2–rGO—dark	0.458	2.74	−2.56	2.11	
TiO_2–rGO—UV	0.479	2.56	−2.71	2.00	−0.129

($[TiO_6]^x$), resulting in electron–hole pair creation as a mono-ionized oxygen vacancy ($[TiO_5.V_o^{\bullet}]$—positive charge) and a negative TiO_2 cluster charged ($[TiO_6]'$) (Eq. 2). Considering UV illumination, then:

$$[TiO_6]^x + hv \rightarrow [TiO_6]' + [TiO_5.V_o^{\cdot}] \quad (2)$$

The first sequence reactions start with the photogenerated mono-ionized oxygen vacancy or positive charge ($[TiO_5.V_o^{\bullet}]$) reacting with surface adsorbed water (H_2O), producing OH* radical and hydrogen ions.

$$[TiO_5.V_o^{\cdot}] + H_2O \rightarrow [TiO_5.V_o^{x}]...OH^*_{(ads)} + H^{\cdot} \quad (3)$$

Di-ionized oxygen vacancy ($[TiO_5.V_o^{\bullet\bullet}]$), formed by reaction between mono-ionized oxygen vacancy ($[TiO_5.V_o^{\bullet}]$) with adsorbed molecular oxygen, could also participate in OH* radical production. However, the main mechanism of OH* production is Eq. 3.

The second step of the mechanism is the photogenerated negative TiO_2 cluster charged ($[TiO_6]'$), or just negative charge reacts with molecular oxygen adsorbed (O_2) on the surface. The hydrogen ions produced during OH* generation ($H^{\bullet}$) (Eq. 3) also participate in the reaction to produce superoxide radicals (O_2H^*).

$$[TiO_6]' + O_2 + H^{\bullet} \rightarrow [TiO_6]^x...O_2H^*_{(ads)} \quad (4)$$

Another possibility to produce O_2H^* radical is the mono-ionized oxygen vacancy ($[TiO_5.V_o^{\bullet}]$) reacts with adsorbed molecular oxygen and hydrogen ions produced during OH* generation, generating O_2H^* radicals. However, the main O_2H^* production is based on Eq. 4.

The RhB discoloration mechanism is influenced by the direct photo-oxidation through the mono-ionized oxygen vacancies ($[TiO_5.V_o^{\bullet}]$) in VB. In this case, mono-ionized oxygen vacancies ($[TiO_5.V_o^{\bullet}]$) reacts with the RhB molecule adsorbed on the semiconductor surface, creating RhB* radical, which will be degraded in subproducts (Eq. 5).

$$[TiO_5.V_o^{\bullet}]...RhB_{(ads)} \rightarrow [TiO_5.V_o^{\bullet}]...RhB^*_{(ads)} \quad (5)$$

Briefly, the RhB degradation mechanism is mainly influenced by three photocatalysis mechanism steps: (i) direct photo-oxidation through the mono-ionized oxygen vacancies (Eq. 5); (ii) OH* radical reaction, mainly produced by photogenerated mono-ionized oxygen vacancy or positive charge ($[TiO_5.V_o^{\bullet}]$) reacting with surface adsorbed water (H_2O) (Eq. 3); (iii) O_2H^* radical reaction, mainly produced by photogenerated negative TiO_2 cluster charged ($[TiO_6]'$) or negative charge reacting with molecular oxygen adsorbed (O_2) (Eq. 4) [46].

By using appropriate scavengers, the formation of ROS species such as hydroxyl (OH*) and superoxide (O_2H^*) radical, as the direct photo-oxidation of oxygen vacancies, were obtained to elucidate the RhB photo-degradation mechanism during UV illumination. The k_s' were obtained using scavengers solution with RhB discoloration process, and the photodegradation reaction kinetics were classified as pseudo-first order reaction (Fig. 3—SI). As the k_s' related to each scavengers solution diminished compared with k' without scavenger solution, the importance of the radical or direct photo-oxidation of oxygen vacancies increases. In other words, it was observed in Table 4 that in the presence of 1,4-benzoquinone (BQ), which is superoxide scavenger, the k_s' was suppressed, indicating that O_2H^* is a reactive oxidative intermediate and influences in the RhB photo-degradation mechanism. In this way, the importance of the step mechanism (IMS) was obtained through the relation:

$$IMS = 100 - \frac{(k_s \times 100)}{k} \quad (6)$$

Which, k_s is the photocatalytic degradation rate values for each scavenger and wavelength illumination, and k is the photocatalytic degradation rate values without scavenger. Tables 4 and 5 depict the k_s values obtained for UV illumination and visible illumination, respectively, for TiO_2, and TiO_2–rGO heterostructure samples, as the SMI values. Figure 9a shows the importance of the step mechanism of discoloration of the RhB under UVC illumination for samples TiO_2, and TiO_2–rGO heterostructure, with the scavengers solutions.

The degradation by the O_2H^* radical is the most important reactive oxygen species for the discoloration of RhB for TiO_2 sample under UV illumination (Fig. 9a). In this case, the primary mechanism step of RhB discoloration for TiO_2 sample under UV illumination is the O_2H^* radical production (Eq. 4). The second most crucial mechanism

Table 4 Photocatalytic degradation rate values under UV illumination obtained by each scavenger solution (ks) and the percentage of importance in photocatalytic mechanism (*SMI* step mechanism importance—Fig. 8)

Scavenger	TiO_2		TiO_2–rGO	
	k_s (min s^{-1}) $\times 10^{-3}$	SMI (%)	k_s (min s^{-1}) $\times 10^{-3}$	SMI (%)
Sec-butanol (BUT)	6.13 ± 0.387	14.62	11.25 ± 0.615	60.91
p-benzoquinone (BQ)	2.16 ± 0.254	69.91	3.30 ± 0.245	82.13
2Na-EDTA (EDTA)	3.27 ± 0.369	54.46	1.68 ± 0.298	90.90

Table 5 Photocatalytic degradation rate values under visible illumination obtained by each scavenger solution (ks) and the percentage of importance in photocatalytic mechanism (*SMI* step mechanism importance—Fig. 8)

Scavenger	TiO_2		TiO_2–rGO	
	k_s (min s^{-1}) $\times 10^{-3}$	SMI (%)	k_s (min s^{-1}) $\times 10^{-3}$	SMI (%)
Sec-butanol (BUT)	7.30 ± 0.105	− 81	6.85 ± 0.258	− 1.03
p-benzoquinone (BQ)	0.72 ± 0.118	82.09	0.59 ± 0.182	91.29
2Na-EDTA (EDTA)	3.25 ± 0.064	19.15	1.11 ± 0.229	83.63

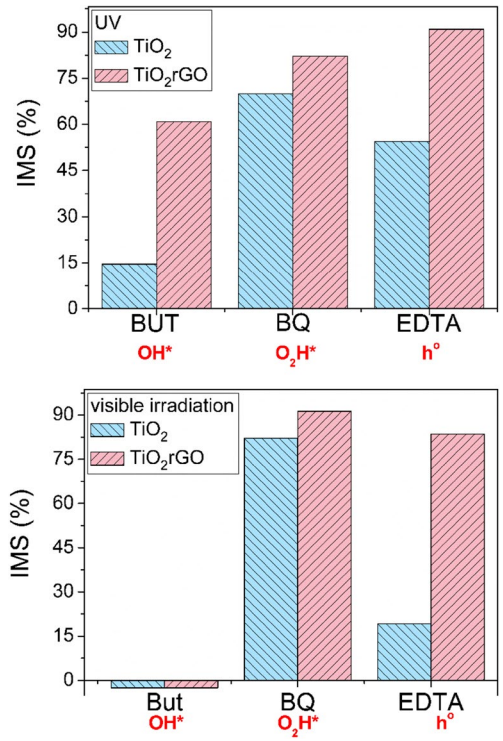

Fig. 9 Discoloration mechanism of Rhod-B under UV and visible illumination of TiO_2 and TiO_2–rGO with scavengers solutions. *But* sec-butanol, *BQ* p-benzoquinone, *EDTA* 2Na-EDTA. Figure based in Tables 4 and 5

step in RhB discoloration for TiO_2 sample under UV illumination is by the direct photo-oxidation by the oxygen vacancies in CB. In this case, oxygen vacancies, $[TiO_5.V_o^{\bullet}]$ reacts with the RhB molecule adsorbed on the semiconductor surface, creating RhB* radical, which will be degraded in subproducts (Eq. 5).

Finally, and the most surprising, the OH* production is the third significant mechanism step in RhB discoloration for TiO_2 sample under UV illumination (Eq. 3). Controversially with the most authors that attribute the major mechanism step for RhB photocatalysis is OH* radical [23, 25, 39, 47]. The half-life time for radicals is generally too small, and inactivation reactions could occur. On the other hand, it is evident that photocharge carrier is created under UV illumination of TiO_2 and, consequently, O_2H* radicals degradation step occurs in the conduction band of the material. In the valence band, the direct photo-oxidation by oxygen vacancies occurs instead of OH* radicals degradation step [8].

The TiO_2–rGO heterostructure formation alters the mechanism of discoloration of RhB under UV illumination since the primary mechanism step responsible for RhB discoloration is through the direct photo-oxidation by oxygen vacancies (Fig. 9a—Eq. 5). In this condition, the photogenerated carriers are created when $[TiO_6]^x$ is UV illuminated (Eq. 2).

TiO_2–rGO heterostructure enables the easily charge separation, attracting the negative charge ($[TiO_6]'$) and trapping it in reduced graphene oxide sheets ($[TiO_6]'\ldots$rGO). Here, an important modification in RhB photocatalytic mechanism compared with TiO_2 sample occurs, when mono-ionized oxygen vacancy ($[TiO_5.V_o^{\bullet}]$) is oxidized to di-ionized oxygen vacancy ($[TiO_5.V_o^{\bullet\bullet}]$) and, then, donates one negative charge to RGO (Eq. 7).

$$[TiO_5.V_o^{\bullet}] + [TiO_6]^x \ldots rGO \rightarrow [TiO_6]' \ldots rGO + [TiO_5.V_o^{\bullet\bullet}] \quad (7)$$

At the same time, the photogenerated positive charge created is trapped as $[TiO_5.V_o^{\bullet\bullet}]$, and the direct photo-oxidation of RhB molecule occurs, representing the most important reactive oxygen species for the discoloration of RhB with TiO_2–rGO heterostructure sample.

The negative photogenerated carrier ($[TiO_6]'$), allocated in rGO sheets, starts the production of O_2H* radical, reacting with adsorbed molecular oxygen (Eq. 8). The O_2H* radical production is the second most important mechanism step in RhB discoloration for TiO_2–rGO heterostructure under UV illumination.

$$[TiO_6]' \ldots rGO + O_2 + H^{\bullet} \rightarrow [TiO_6]^x \ldots rGO \ldots O_2H^*_{(ads)} \quad (8)$$

Finally, the OH* production takes place with photogenerated mono-ionized oxygen vacancy or positive charge ($[TiO_5.V_o^{\bullet}]$) reacting with surface adsorbed water (H_2O) (Eq. 2), and producing OH* radical and hydrogen. Another important factor that collaborates with the main mechanism step of RhB discoloration by TiO_2–rGO heterostructure

under UV illumination is the possibility to rGO increase the RhB molecules adsorption over the surface material, which facilities the direct photo-oxidation by oxygen vacancies.

Figure 9b presents the photocatalysis process with scavengers solution under visible illumination for TiO_2 and TiO_2–rGO heterostructure samples. Under visible light, the dye sensitizing mechanism takes place, where the RhB molecule could be excited through visible wavelength absorption (RhB*) due to the color characteristics, and reacts with the TiO_2 neutral cluster ($[TiO_6]^x$), transferring a negative charge and creating negatively charged cluster ($[TiO_6]'$). Also, as RhB donates a negative charge, a positive charge is created on the RhB molecule (RhB^+).

$$[TiO_6]^x + RhB^* \rightarrow [TiO_6]' + RhB^+ \quad (9)$$

Although the above reaction plays an important factor and starts the RhB discoloration mechanism under visible illumination, Fig. 9b shows the most reactive oxygen species for RhB discoloration mechanism under visible illumination is O_2H* radical (Eq. 4, Fig. 4—SI). The But scavenger results depict SMI with negative values and should not be considerate at this moment. The second most important step is the direct photo-oxidation of RhB by oxygen vacancies (Eq. 5), and the last important is the OH* production (Eq. 3). The butanol scavenger solution shows an increase in k_s' value higher than k′ without any scavenger and presents a negative SMI. With OH* radical scavenger (butanol) in the RhB solution, the photo-charge separation is forced, inhibiting the RhB discoloration through OH* radical step (Eq. 3). As O_2H* radical is the most important reactive oxygen species in the RhB degradation mechanism for TiO_2 sample, the k_s' value related to butanol scavenger increase more than k′ without scavenger. It is important to notice that, although the visible mechanism steps could be similar for TiO_2 under visible and UV illumination, the efficiency of each mechanism step for visible illumination is lower than in UV illumination mechanism, as represented by k_s' values.

Under visible light, the TiO_2–rGO heterostructure did not necessarily alter the major mechanism step of RhB discoloration compared to TiO_2 sample. It is proposed that the rGO only favor such steps, especially the charge transfer steps showed in the single equation, and, consequently, influences in the ROS production. The RhB discoloration mechanism for TiO_2–rGO heterostructure under visible illumination suffers influence by dye sensitizing mechanism similar to the TiO_2 mechanism. Additionally, the rGO promotes other electron transfer to conducting a band of TiO_2 as it presents broad absorption under visible illumination [26], allowing the rGO excitation under visible light (rGO*) equation, as presented by DRS results. In this way, excited RhB molecule (Eq. 9) and rGO (Eq. 10) increase the production of O_2H* radical in the mechanism

$$[TiO_6]^x + rGO^* \rightarrow [TiO_6]' + rGO^+ \quad (10)$$

Particularly, in the case of rGO* under visible illumination, it is possible that the efficiency of O_2H radical production through the reaction with the negative photogenerated carrier ($[TiO_6]'$), allocated in rGO sheets, with adsorbed molecular oxygen (Eq. 8), is more elevated than the reaction between the negative TiO_2 cluster charged ($[TiO_6]'$) with molecular oxygen adsorbed (Eq. 4), which occur in TiO_2 sample. The promoted photo-carrier separation effect produced by TiO_2–rGO heterostructure enables the direct photo-oxidation of RhB by oxygen vacancies (Eq. 6), being the second more important steps in RhB mechanism under visible illumination. However, the importance of the direct photo-oxidation by the oxygen vacancies is higher for TiO_2–rGO heterostructure than for TiO_2 sample, promoting an increase in visible photocatalysis of TiO_2–rGO heterostructure sample.

The essential RhB degradation mechanism steps under UV and visible illumination for TiO_2 and TiO_2–rGO heterostructure samples is illustrated in Fig. 10, and are based on an equation from 2 to 10. Reduced graphene oxide (rGO) is well known as a useful charge intermediate [46, 48, 49]. The PL results show that TiO_2–rGO heterostructure inhabits the charge carrier recombination and electrochemical results show that TiO_2–rGO heterostructure presents a faster electron transfer than TiO_2 samples. The first index (1) indicates the photo-charge creation (Eq. 2) in every condition. The index 2 indicates the most critical RhB degradation mechanism steps for each condition. The following index illustrates the classification in importance for every reactive oxygen species in RhB degradation mechanism.

4 Conclusion

The RhB discoloration mechanism was proposed for TiO_2 nanoparticles and TiO_2–rGO heterostructure. The TiO_2–rGO heterostructure formation modifies the main reactive oxygen species and, consequently, modifies de mechanism compared with TiO_2 nanoparticles sample, under UV and visible illumination. For TiO_2–rGO heterostructure, the synthesis medium changes the morphology of the sample. The FE-SEM analysis exhibit TiO_2 with around 6.0 nm in diameter and the presence of rGO increase the crystallite size confirmed by Scherrer equation. However, the specific surface decrease with the heterostructure creation. The non-hydrolytic method favors a better distribution of TiO_2 nanoparticles around the rGO

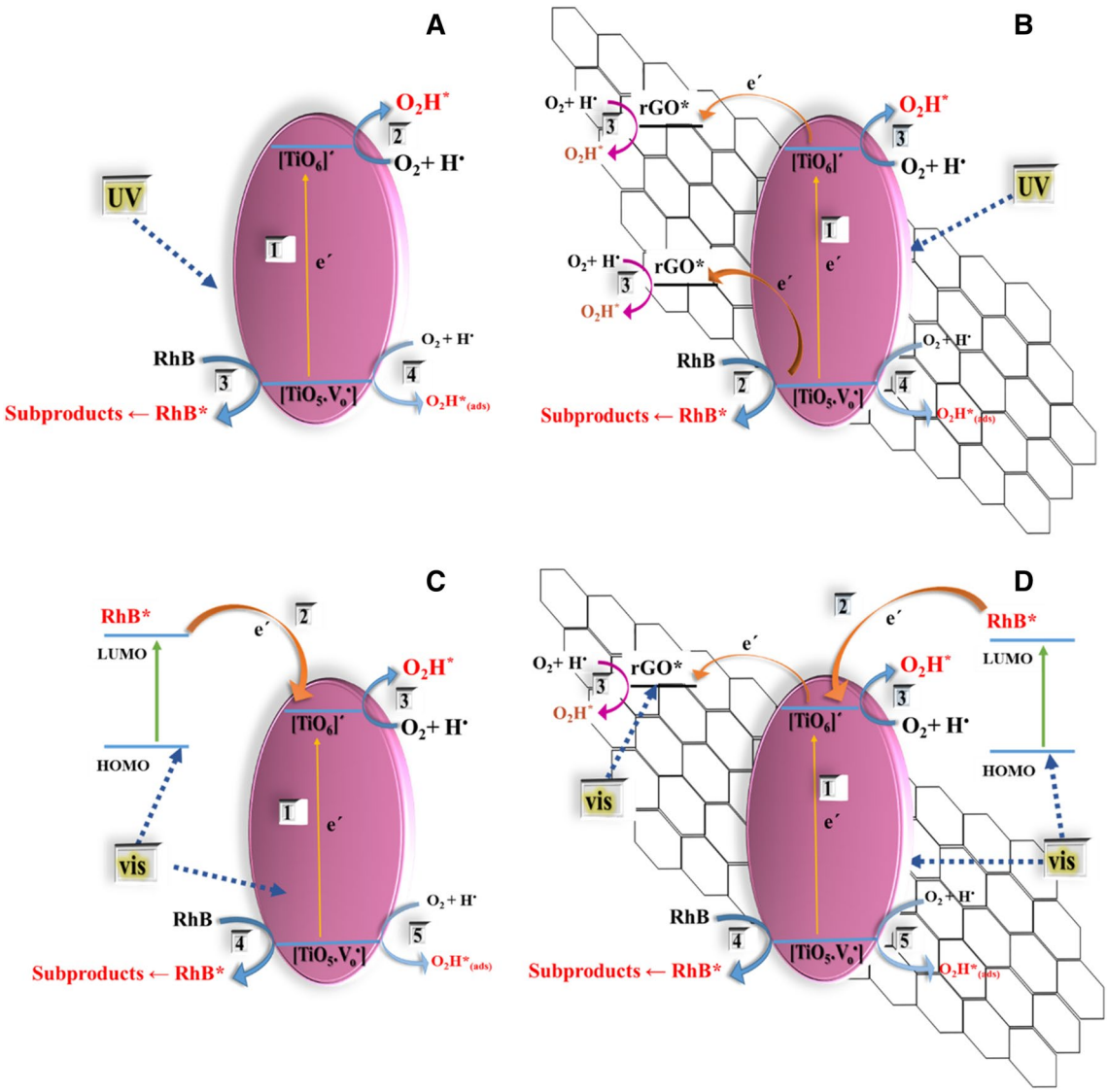

Fig. 10 Scheme of proposed RhB discoloration for TiO_2 under UV (**a**) and visible (**c**) illumination and for TiO_2–rGO under UV (**b**) and visible (**d**) illumination. The numbers indicated the sequence which steps mechanism occurs

structure, due to the alteration of functional groups caused by the organic solvent. The two samples show the anatase crystalline phase TiO_2. However, the heterostructure decreased the band gap of the samples. It can be observed that TiO_2–rGO heterostructure increases the efficiency in the RhB photocatalytic degradation under UVC illumination, promoting a better separation of photogenerated charges than the TiO_2 sample. The improvement of photocatalytic efficiency of TiO_2–rGO heterostructure compared with TiO_2 sample is caused by diverse factors: (i) morphology, which shows well dispersed TiO_2 nanoparticles homogeneous distributed all over the rGO sheet; (ii) rGO reduction characteristics; (iii) the intense absorption in the visible light region; (iv) the decrease in band gap values; (v) the inhibition of the charge carrier recombination and (vi) the faster electron transfer. The RhB discoloration mechanism modifications for the TiO_2–rGO heterostructure are presented, and the primary reactive oxygen species production is changed.

Acknowledgements The authors acknowledge São Paulo Research Foundation (FAPESP), grant #CEPID 2013/07296-2, grant #2015/04511-5, grant #2014/17343-0, grant #2017/01267-1, grant #2012/26671-9. National Council for Scientific and Technological Development – CNPQ, grant #444926/2014-3. Authors thank Dr. Carlos J.L. Constantino and her student Sabrina A. Camacho for Raman measurements (FAPESP grant #2014/11410-8).

Compliance with ethical standards

Conflict of interest On behalf of all authors, the corresponding author states that there is no conflict of interest.

References

1. F. Pei, S. Xu, W. Zuo et al., Effective improvement of photocatalytic hydrogen evolution via a facile in-situ solvothermal N-doping strategy in N-TiO_2/N-graphene nanocomposite. Int. J. Hydrog. Energy **39**, 6845–6852 (2014). https://doi.org/10.1016/j.ijhydene.2014.02.173
2. P. Fernández-Ibáñez, M.I. Polo-López, S. Malato et al., Solar photocatalytic disinfection of water using titanium dioxide graphene composites. Chem. Eng. J. **261**, 36–44 (2014). https://doi.org/10.1016/j.cej.2014.06.089
3. S. Huang, Z. Si, X. Li et al., A novel Au/r-GO/TNTs electrode for H_2O_2, O_2 and nitrite detection. Sen. Actuators B **234**, 264–272 (2016). https://doi.org/10.1016/j.snb.2016.04.167
4. Q. Xiang, B. Cheng, J. Yu, Graphene-based photocatalysts for solar-fuel generation. Angew Chem. Int. Ed. (2015). https://doi.org/10.1002/anie.201411096
5. Q. Xiang, J. Yu, M. Jaroniec, Graphene-based semiconductor photocatalysts. Chem. Soc. Rev. **41**, 782 (2012). https://doi.org/10.1039/c1cs15172j
6. J. Liu, H. Bai, Y. Wang et al., Self-assembling TiO_2 nanorods on large graphene oxide sheets at a two-phase interface and their anti-recombination in photocatalytic applications. Adv. Funct. Mater. **20**, 4175–4181 (2010). https://doi.org/10.1002/adfm.201001391
7. A.H. Cheshme Khavar, G. Moussavi, A.R. Mahjoub, The preparation of TiO_2@rGO nanocomposite efficiently activated with UVA/LED and H_2O_2 for high rate oxidation of acetaminophen: catalyst characterization and acetaminophen degradation and mineralization. Appl. Surf. Sci. **440**, 963–973 (2018). https://doi.org/10.1016/j.apsusc.2018.01.238
8. N. Sun, J. Ma, C. Wang et al., A facile and efficient method to directly synthesize TiO_2/rGO with enhanced photocatalytic performance. Superlatt. Microstruct. **121**, 1–8 (2018). https://doi.org/10.1016/J.SPMI.2018.07.017
9. M. Dhanasekar, V. Jenefer, R.B. Nambiar et al., Ambient light antimicrobial activity of reduced graphene oxide supported metal doped TiO_2 nanoparticles and their PVA based polymer nanocomposite films. Mater. Res. Bull. **97**, 238–243 (2018). https://doi.org/10.1016/j.materresbull.2017.08.056
10. A.V.F.M.V. Ramana, R.S.T. Jadhav, G.S.G. Dae, Y. Kim, TiO_2/reduced graphene oxide composite based nano-petals for supercapacitor application: effect of substrate. J. Mater. Sci. (2018). https://doi.org/10.1007/s10854-018-9146-5
11. B. Chai, J. Li, Q. Xu, K. Dai, Facile synthesis of reduced graphene oxide/WO_3 nanoplates composites with enhanced photocatalytic activity. Mater. Lett. **120**, 177–181 (2014). https://doi.org/10.1016/j.matlet.2014.01.094
12. M. Long, Y. Qin, C. Chen et al., Origin of visible light photoactivity of reduced graphene oxide/TiO_2 by in situ hydrothermal growth of undergrown TiO_2 with Graphene Oxide. J. Phys. Chem. C **117**, 16734–16741 (2013)
13. M. Andreozzi, M.G. Álvarez, S. Contreras et al., Treatment of saline produced water through photocatalysis using rGO–TiO_2 nanocomposites. Catal Today (2018). https://doi.org/10.1016/j.cattod.2018.04.048
14. Y. Yuan, Y. Leigh, A. Xuchuan, Experimental and theoretical studies of gold nanoparticle decorated zinc oxide nanoflakes with exposed {10 0} facets for butylamine sensing. Sens. Actuators B (2016). https://doi.org/10.1016/j.snb.2016.02.091
15. D. Chen, H. Zhang, S. Hu, J. Li, Preparation and enhanced photoelectrochemical performance of coupled bicomponent ZnO–TiO_2 nanocomposites. J. Phys. Chem. C **112**, 117–122 (2008). https://doi.org/10.1021/jp077236a
16. A. Habib, T. Shahadat, N.M. Bahadur et al., Synthesis and characterization of ZnO–TiO_2 nanocomposites and their application as photocatalysts. Int. Nano Lett. **3**, 1–8 (2013). https://doi.org/10.1186/2228-5326-3-5
17. A.K. Geim, K.S.S. Novoselov, The rise of graphene. Nat. Mater. **6**, 183–191 (2007). https://doi.org/10.1038/nmat1849
18. A.K. Geim, Graphene: status and prospects. Science **324**, 1530–1534 (2009). https://doi.org/10.1126/science.1158877
19. D.P. Volanti, D. Keyson, J.A. Varela, E. Longo, Aparato assistido por microondas para síntese hidrotérmica de óxidos nanoestruturados. Universidade Estadual Paulista And Universidade Federal de São Carlos (Brasil). Br N. Pi0815393-0 07 Dez. 2010 (2008)
20. G.B. Soares, B. Bravin, C.M.P. Vaz, C. Ribeiro, Facile synthesis of N-doped TiO_2 nanoparticles by a modified polymeric precursor method and its photocatalytic properties. Appl. Catal. B **106**, 287–294 (2011). https://doi.org/10.1016/j.apcatb.2011.05.018
21. M. Dawson, G.B. Soares, C. Ribeiro, Influence of calcination parameters on the synthesis of N-doped TiO_2 by the polymeric precursors method. J. Solid State Chem. **215**, 211–218 (2014). https://doi.org/10.1016/j.jssc.2014.03.044
22. S.A. Bakar, G. Byzynski, C. Ribeiro, Synergistic effect on the photocatalytic activity of N-doped TiO_2 nanorods synthesised by novel route with exposed (110) facet. J. Alloys Compd. **666**, 38–49 (2016). https://doi.org/10.1016/j.jallcom.2016.01.112
23. H. Wang, H. Gao, M. Chen et al., Microwave-assisted synthesis of reduced graphene oxide/titania nanocomposites as an adsorbent for methylene blue adsorption. Appl. Surf. Sci. **360**, 840–848 (2016). https://doi.org/10.1016/j.apsusc.2015.11.075
24. F. Liu, X. Yan, X. Chen et al., Mesoporous TiO_2 nanoparticles terminated with carbonate-like groups: amorphous/crystalline structure and visible-light photocatalytic activity. Catal. Today **264**, 243–249 (2016). https://doi.org/10.1016/j.cattod.2015.07.012
25. K.H. Leong, L.C. Sim, D. Bahnemann et al., Reduced graphene oxide and Ag wrapped TiO_2 photocatalyst for enhanced visible light photocatalysis. Appl. Mater. **3**, 104503 (2015). https://doi.org/10.1063/1.4926454
26. M.Q. Yang, Y.J. Xu, Basic principles for observing the photosensitizer role of graphene in the graphene-semiconductor composite photocatalyst from a case study on graphene-ZnO. J. Phys. Chem. C **117**, 21724–21734 (2013). https://doi.org/10.1021/jp408400c
27. J. Qin, X. Zhang, C. Yang et al., ZnO microspheres-reduced graphene oxide nanocomposite for photocatalytic degradation of methylene blue dye. Appl. Surf. Sci. (2016). https://doi.org/10.1016/j.apsusc.2016.09.043
28. Y. Zhang, C. Xie, F.L. Gu et al., Significant visible-light photocatalytic enhancement in Rhodamine B degradation of silver orthophosphate via the hybridization of N-doped graphene and poly(3-hexylthiophene). J. Hazard. Mater. **315**, 23–34 (2016). https://doi.org/10.1016/j.jhazmat.2016.04.068
29. L.-L. Tan, W.-J. Ong, S.-P. Chai et al., Visible-light-active oxygen-rich TiO_2 decorated 2D graphene oxide with enhanced photocatalytic activity toward carbon dioxide reduction. Appl. Catal. B **179**, 160–170 (2015). https://doi.org/10.1016/j.apcatb.2015.05.024
30. A. Ambrosi, M. Pumera, Electrochemically exfoliated graphene and graphene oxide for energy storage and electrochemistry applications. Chem. A **22**, 153–159 (2016). https://doi.org/10.1002/chem.201503110
31. K. Dhara, T. Ramachandran, B.G. Nair, T.G. Satheesh Babu, Single step synthesis of Au–CuO nanoparticles decorated reduced graphene oxide for high performance disposable nonenzymatic

glucose sensor. J. Electroanal. Chem. **743**, 1–9 (2015). https://doi.org/10.1016/j.jelechem.2015.02.005
32. H. Yang, C. Shan, F. Li et al., Covalent functionalization of polydisperse chemically-converted graphene sheets with amine-terminated ionic liquid. Chem. Commun. (2009). https://doi.org/10.1039/b905085j
33. X. Bai, C. Sun, D. Liu et al., Photocatalytic degradation of deoxynivalenol using graphene/ZnO hybrids in aqueous suspension. Appl. Catal. B **204**, 11–20 (2017). https://doi.org/10.1016/j.apcatb.2016.11.010
34. H. Sun, S. Liu, S. Liu, S. Wang, A comparative study of reduced graphene oxide modified TiO_2, ZnO and Ta_2O_5 in visible light photocatalytic/photochemical oxidation of methylene blue. Appl. Catal. B **146**, 162–168 (2014). https://doi.org/10.1016/j.apcatb.2013.03.027
35. M.E.D.G. Azenha, H.D. Burrows, L.M. Canle et al., Kinetic and mechanistic aspects of the direct photodegradation of atrazine, atraton, ametryn and 2-hydroxyatrazine by 254 nm light in aqueous solution. J. Phys. Org. Chem. **16**, 498–503 (2003). https://doi.org/10.1002/poc.624
36. W. Wang, J. Yu, Q. Xiang, B. Cheng, Enhanced photocatalytic activity of hierarchical macro/mesoporous TiO_2-graphene composites for photodegradation of acetone in air. Appl. Catal. B **119–120**, 109–116 (2012). https://doi.org/10.1016/j.apcatb.2012.02.035
37. K. Zhou, Y. Zhu, X. Yang et al., Preparation of graphene–TiO_2 composites with enhanced photocatalytic activity. N. J. Chem. **35**, 353–359 (2011)
38. V.R. Posa, V. Annavaram, J.R. Koduru et al., Preparation of graphene–TiO_2 nanocomposite and photocatalytic degradation of Rhodamine-B under solar light irradiation. J. Exp. Nanosci. **11**, 722–736 (2016). https://doi.org/10.1080/17458080.2016.1144937
39. G. Peng, J.E. Ellis, G. Xu et al., In situ grown TiO_2 nanospindles facilitate the formation of holey reduced graphene oxide by photodegradation. ACS Appl. Mater. Interfaces **8**, 7403–7410 (2016). https://doi.org/10.1021/acsami.6b01188
40. G. Byzynski, C. Ribeiro, E. Longo, Blue to yellow photoluminescence emission and photocatalytic activity of nitrogen doping in TiO_2 powders. Int. J. Photoenergy (2015). https://doi.org/10.1155/2015/831930
41. E. Cui, G. Lu, Enhanced surface electron transfer by fabricating a core/shell Ni@NiO cluster on TiO_2 and its role on high efficient hydrogen generation under visible light irradiation. Int J Hydrog. Energy **39**, 8959–8968 (2014). https://doi.org/10.1016/j.ijhydene.2014.03.258
42. D. Martín-Yerga, E.C. Rama, A. Costa-García, Electrochemical characterization of ordered mesoporous carbon screen-printed electrodes. J. Electrochem. Soc. **163**, B176–B179 (2016). https://doi.org/10.1149/2.0871605jes
43. Soares GB, Ribeiro RAP, De Lazaro SR, Ribeiro C, Photoelectrochemical and theoretical investigation of the photocatalytic activity of TiO_2: N. RSC Adv. (2016). https://doi.org/10.1039/c6ra15825k
44. J. Low, J. Yu, M. Jaroniec et al., Heterojunction photocatalysts. Adv. Mater. (2017). https://doi.org/10.1002/adma.201601694
45. G.B. Soares, R.A.P. Ribeiro, S.R. de Lazaro, C. Ribeiro, Photoelectrochemical and theoretical investigation of the photocatalytic activity of TiO_2: N. RSC Adv. (2016). https://doi.org/10.1039/c6ra15825k
46. P. Wang, S. Zhan, Y. Xia et al., The fundamental role and mechanism of reduced graphene oxide in rGO/Pt–TiO_2 nanocomposite for high-performance photocatalytic water splitting. Appl. Catal. B **207**, 335–346 (2017). https://doi.org/10.1016/j.apcatb.2017.02.031
47. K.S. Divya, M.M. Xavier, P.V. Vandana et al., A quaternary TiO_2/ZnO/RGO/Ag nanocomposite with enhanced visible light photocatalytic performance. N. J. Chem. **41**, 6445–6454 (2017). https://doi.org/10.1039/C7NJ00495H
48. Y. Yang, Q. Jin, D. Mao et al., Dually ordered porous TiO_2–rGO composites with controllable light absorption properties for efficient solar energy conversion. Adv. Mater. (2016). https://doi.org/10.1002/adma.201604795
49. X. Li, R. Shen, S. Ma et al., Graphene-based heterojunction photocatalysts. Appl. Surf. Sci. **430**, 53–107 (2018). https://doi.org/10.1016/j.apsusc.2017.08.194